Randomness in a Galton board from the viewpoint of predictability: Sensitivity and statistical bias of output states

Kenichi Arai,* Takahisa Harayama, Satoshi Sunada, and Peter Davis
NTT Communication Science Laboratories, NTT Corporation, 2-4 Hikaridai, Seika-cho, Soraku-gun, Kyoto 619-0237, Japan
(Received 12 October 2011; revised manuscript received 4 June 2012; published 27 November 2012)

The Galton board is a classic example of the appearance of randomness and stochasticity. In the dynamical model of the Galton board, the macroscopic motion is governed by deterministic equations of motion, and predictability depends on uncertainty in the initial conditions and its evolution by the dynamics. In this sense the Galton board is similar to coin tossing. In this paper, we analyze a simple dynamical model which is inspired by the Galton board. Especially, we focus on the predictability, considering the relation between the uncertainty of initial states and the structure of basins of initial states that result in the same exit state. The model has basins with fractal basin structure, unlike the basins in coin tossing models which have only finite structure. Arbitrarily small uncertainty of initial conditions can cause unpredictability of final states if the initial conditions are chosen in fractal regions. In this sense, our model is in a different category from the coin tossing model. We examine the predictability of a small Galton board model from the viewpoint of the sensitivity and the statistical bias of final states. We show that it is possible to determine the radii of scatterers corresponding to a given predictability criterion, specified as a statistical bias, and a given uncertainty of initial conditions.

DOI: 10.1103/PhysRevE.86.056216 PACS number(s): 05.45.Ac

I. INTRODUCTION

Random sequence generators are key technologies for ciphers [1] and numerical simulations [2,3]. Various algorithms executed in computers and physical devices using thermal or quantum noise have been developed to generate random sequences. Algorithms such as the linear congruential generator [4] and the Mersenne twister [5] can be used to generate so-called pseudorandom sequences in computers. These pseudorandom sequences are completely reproducible if we know the algorithm and the seeds of the sequences, and on a finite state computer they are eventually periodic, although pseudorandom sequences of finite length can be difficult to distinguish from sequences generated by a truly random sequence generator. However, pseudorandom sequences are not suitable for some security applications which rely on the nonreproducibility of sequences. On the contrary, unreproducible random sequences can be obtained using well-designed physical devices.

Typically, practical physical devices which are used to produce unreproducible and unpredictable random sequences are dynamical randomizers, which make use of complicated dynamical behavior together with some kind of inherent uncertainty. Mechanical randomizers such as coin tossing and dice throwing are examples of dynamical randomizers. Their motions are modeled with a deterministic dynamical system governed by Newton's laws, but they also have nondeterministic properties such as uncertainty of the initial configuration and the effects of environmental noise. Generation of random sequences using nonmechanical dynamical randomizers based on electronic and optical devices has been proposed. For example, a method to generate random sequences using chaotic semiconductor lasers has recently been proposed [6,7], which achieves very high generation rates.

Dynamical randomizers can be distinguished into two categories from the view point of output sequence lengths. In one case the output is an unbounded sequence, while in the other it is bounded. Periodically repeated measurements on a steady system, such as devices using chaotic semiconductor lasers, provide examples of the first category. Coin tossing and dice throwing are typical examples of the second category since their outputs are a finite set of states. The Galton board [8] is also classified into this category. It consists of pegs arranged on a vertical board in a hexagonal array. There is a funnel at the top of the board, and balls are thrown into the board through the funnel. In the lower part of the board, there is a number of slots which are divided by slats. The balls fall under the influence of gravity, bouncing off pegs on their way down. Eventually, the balls fall into one of the slots at the bottom of the device. The balls collect in the slots at the bottom, and the distribution of the balls is typically close to a binomial distribution, which approaches a Gaussian distribution for a large sized board, consistent with the "laws of probabilities" [9]. In this sense, although coins, dice, and the Galton board are all mechanical randomizers and their outputs are bounded, the determination of the final states of the Galton board are somewhat different from the coin and dice cases, where the final state is determined by the coin or dice spontaneously coming to rest.

Due to the complicated motion of coins and dice, any ambiguity in the knowledge of the state is amplified, and the final states become difficult to predict. It is natural to conjecture that chaotic motion plays an important role in the complicated motion of mechanical randomizers and hence in the predictability of the final state. The pioneering work by Keller revealed that the preimages of heads are simple [10], and Vulović and Prange reported numerical experiments showing that coins are not unpredictable due to the finite size of basins [11]. Some authors investigated the randomness in the coin toss more precisely but agreed with the predictability of the outcome of coin tossing [12–15]. Nagler and Richter revealed that the same is true for dice throwing [16].

*arai.k@lab.ntt.co.jp

In this paper, we discuss the randomness in the ideal Galton board, which has not yet been studied from the point of view of random output generation, although some features of the Galton board have been studied from the view point of a model of physical materials [17–22]. We deal with an ideal dynamical model which is inspired by the Galton board. There are some difference in behaviors between the dynamical model and real physical devices, as discussed later. In our Galton board model, point particles fall, deterministically governed by the Newton's laws of motion, and some uncertainty of the initial condition is supposed to be unavoidable in the same way as coin tossing and dice throwing. A statistical distribution of initial states representing the uncertainty of initial conditions is deterministically mapped into a discrete set of final states in a way such that the final states become nondeterministic, or stochastic. Suppose that initial states are independently picked from a distribution which characterizes the initial uncertainty. Then the corresponding final states are also independent, but their distributions depend on the dynamical evolution. It may be that we always have the same final state even with the uncertainty of the initial conditions, and so we can predict the final state completely. This is related to the sensitivity of the final state [23,24]. Or it may be that the final state is not completely predictable but the distribution of the final states is strongly biased, so that the final state can be predicted with high probability. On the other hand, when the distribution of final states is evenly distributed, then they are "completely" unpredictable, and we obtain true randomness. The statistical bias is the key to the predictability of the final states and the robustness of final state distributions. In this paper, we study the predictability of the Galton board model, specifically in terms of the sensitivity and the statistical bias of the distributions of the final states.

The dynamical behavior of the Galton board is related to the phenomenon known as chaotic scattering [25]. In scattering systems, particles enter a scattering domain, interact with scatterers, and then leave the domain. The dependence of the departure states on the entry states is typically very complicated. A chaos mirror [26] has been proposed as an application of chaotic scattering in which a small change in the input ray direction results in a complicated change in the output ray direction. The chaotic nature of scattering has been well studied in so-called billiard systems in which point particles bounce elastically among a set of scatterers. The billiard system corresponds to the physical model known as the Lorentz gas. Barra *et al.* [22] studied the Galton board model as a Lorentz gas with a uniform external field and showed the nonequilibrium stationary density under the conditions of absorbing boundaries and stochastic injection of particles. In addition, the density of collisions on the Birkhoff coordinates of each disk is shown to have fractality, and the fractality is shown to be the key to a positive entropy production rate. Bleher *et al.* showed the fractality of a billiard system with exits through one of which an orbit can escape from the system [23]. In this paper, we investigate the fractality of the Galton board model from the view point of the predictability of output states. The predictability depends on the sensitivity of final states, which is deeply affected by the relation between the uncertainty of the initial states and the structures of the dynamical basins that connect the initial states and the final states.

In this paper we will discuss the difference between a Galton board model with coin tossing and dice throwing models. There are differences between a Galton board and coin tossing or dice throwing models from the viewpoint of how to determine output states. In coin tossing, outputs are determined by the final states of a coin when it is caught by the hands, that is to say, a compulsive termination. In dice throwing, outputs are determined by the final states of a die when its energy becomes too low to continue to roll. With the compulsive termination or the energy dissipation, the motions of coins or dice are finite; otherwise, the outputs of coins and dice cannot be obtained. In the Galton board model it is possible to determine the output states even without dissipation by defining the output states as the exits of the pin region. In a Galton board model without dissipation there can be arbitrarily long trajectories and an arbitrarily fine fractal structure, which affects the sensitivities of the final states. A real Galton board has energy dissipation, but its behavior approaches an ideal model by carefully setting up an experimental system and refining the experimental conditions. There can be significant differences between the Galton board with no dissipation and coin tossing with dissipation since the basin can have fractal structures. We describe the difference between the Galton board model and coin tossing from the point of view of mechanical randomizers.

We briefly mention the difference between the mathematical model of an ideal Galton board and a real physical Galton board. We consider a point particle with no rotational degrees of freedom. We suppose no energy dissipation in our model, that is, no air resistance and completely elastic collision. In addition, trajectories are exposed to no fluctuation along the way, and thus trajectories are determined by initial conditions picked from some statistical ensemble and a deterministic equation of motion.

In Sec. II, we describe the mathematical model of the Galton board and the way to trace the trajectories numerically. We focus our attention on a small Galton board model. In Sec. III, we show the fractal basin structures. Then, we investigate the relation between the structure of basins and the initial uncertainty from the point of view of two aspects of unpredictability. One is the final state sensitivity, studied in Sec. IV, and the other is the statistical bias, studied in Sec. V. Finally, we summarize the work in Sec. VI.

II. GALTON BOARD MODEL

The schematic of a Galton board apparatus, whose appearance is inherited from the image of a Galton board introduced by Kac [9], is shown in Fig. 1(a). The balls' motions are restricted to the two-dimensional space, and there are walls on both sides so that particles do not go too far in the lateral direction. In a real Galton board balls bounce off pegs as they fall. For ease of computation, we consider an equivalent dynamical model of a Galton board where point particles bounce off circular disks fixed on a plane, as in previous works [17–22]. Particles fall under the influence of a constant gravitational field and elastically bounce off circular disks arranged in a hexagonal array, as shown in Fig. 1(b). The positions of pegs and centers of balls correspond to the centers of disk scatterers and the positions of point particles, respectively. In addition, the radius of disk scatterers corresponds to that of

balls in the real Galton board. The line segments connecting the outermost disks in Fig. 1(b) correspond to the side walls in Fig. 1(a). The line segments are arranged in parallel with the side walls, and the distance between them is equal to the radius of disk scatterers. The trajectories of both figures are completely equivalent if we ignore the rotation of balls in Fig. 1(a). Our model also excludes the effects of thermal and quantum fluctuations during the motion.

We introduce an orthogonal coordinate system O_{xy}. The direction of the x axis is horizontal and perpendicular to the gravity direction, and the y axis is vertical and opposite to the direction of gravity. The distance between the centers of nearest neighbor circular disks is 2, and their radii are r. The side reflecting segments are placed along the lines $y = \pm\sqrt{3} + \sqrt{3}$. The mass of a particle is supposed to be 1 for the sake of simplicity. Particles are released from between the two uppermost scatterers, which we call the "entrance."

Particles fall obeying Newton's equation of motion with gravitational acceleration $g = 9.8$; $\ddot{x} = 0$ and $\ddot{y} = -g$. Since the collision of a particle and a circular disk is completely elastic, there is no energy dissipation in our model, and the total energy is always preserved:

$$E = \tfrac{1}{2}|\boldsymbol{v}(t)|^2 + gy(t) = \text{const.} \tag{1}$$

Here, we describe how to calculate the trajectories of particles numerically. A particle with an initial position (x_0, y_0) and an initial velocity (u_x, u_y) falls freely in a parabola. The free fall will be interrupted by one of the following events: it collides with a side reflecting line or a disk scatterer or exits from the domain. Tracing trajectories of a collision with a reflecting line is relatively simple. Let us describe the case in which a particle reflects off a disk scatterer. Suppose that τ seconds later, the particle will collide with a disk scatterer whose center is (x_c, y_c). τ satisfies the following quartic equation:

$$\begin{aligned}&\frac{g^2}{4}\tau^4 - gu_y\tau^3 + \left[u_x^2 + u_y^2 - g(y_0 - y_c)\right]\tau^2 \\ &\quad + 2[u_x(x_0 - x_c) + u_y(y_0 - y_c)]\tau \\ &\quad + (x_0 - x_c)^2 + (y_0 - y_c)^2 - r^2 = 0.\end{aligned} \tag{2}$$

We obtain four values of τ by solving the quartic formula numerically with Class Library for Numbers [27]. The smallest positive value of τ is the desired solution for the time interval τ to the next collision. The position (x_i, y_i) and velocity (v_x, v_y) of the particle just before the next collision can be calculated using τ as

$$\begin{aligned}x_i &= u_x\tau + x_0, \quad y_i = -\tfrac{1}{2}g\tau^2 + u_y\tau + y_0, \\ v_x &= u_x, \quad v_y = -g\tau + u_y.\end{aligned}$$

Letting u'_x and u'_y be the horizontal and vertical velocities of the particle just after collision, respectively, then, we have the following relations:

$$u'_x = v_x(\cos^2\alpha - \sin^2\alpha) + 2v_y \sin\alpha\cos\alpha, \tag{3}$$

$$u'_y = 2v_x \sin\alpha\cos\alpha + v_y(\sin^2\alpha - \cos^2\alpha), \tag{4}$$

where α denotes the angle between the y axis and the outward normal of the circle at the impact point (x_i, y_i). After the collision the particle will fall freely again, starting with the initial position (x_i, y_i) and the initial velocity (u'_x, u'_y). By repeating calculations of reflecting off a disk scatterer or a side wall, we can trace the particle's trajectory.

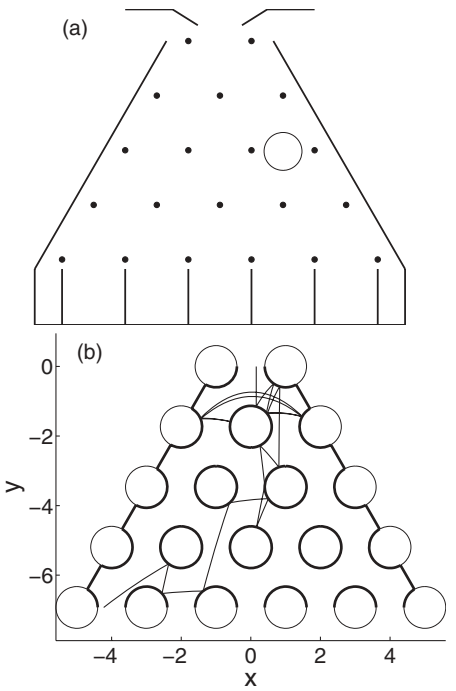

FIG. 1. (a) Schematic of the Galton board apparatus. (b) Model of the Galton board in the orthogonal coordinate system. The radii of circular disks are $r = 0.60$, and the distance between the centers of the nearest circular disks is 2. An example of a trajectory of a particle falling and bouncing off circular disks is shown.

Finally, particles exit from one of the spaces between two scatterers in the bottom row, which we call an exit. The exit which a particle passes through is used to define a final coarse-grained state of the particle. The domain surrounded by the entrance, the exits, and side walls, where particles free fall and repeatedly bounce off scatterers, is referred to as the scattering domain.

A. Small Galton board model

We would like to deal with a Galton board model with a small number of scatterers for the sake of simplicity. We consider a Galton board model with a relatively small number of scatterers, as shown in Fig. 2. This model is a single-storied Galton board model, while the model shown in Fig. 1 is a multistoried Galton board model. We refer to this as a small Galton board model. This model has a sufficient number of scatterers in the following sense. Even in this small model, uncertainty about the initial state in the entrance can result in trajectories to more than one final state, the right or left exit. Thus, this small Galton board model can produce an elementary process of randomness. A set of five disks in two rows, with two disks in the top row and three disks in the bottom row, forming a scattering region with one entrance and two exists, is the simplest section of a Galton board showing the generation of random output, in the sense that trajectories from the entrance can split irreversibly into two groups passing through separate exits. In this small model, we will show the existence of fractal structures of basins and the dependence of

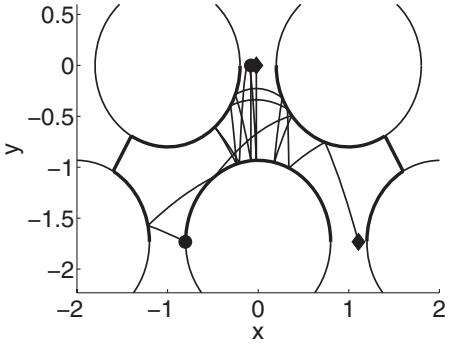

FIG. 2. Small Galton board model for $r = 0.80$. Two particles are released from the entrance and bounce off the circular elastic surfaces many times. One passes out through the right exit, and the other gets out through the left exit. The bold lines show reflecting surfaces in the model.

the bias of final states. Clarifying these properties is essential to understanding the randomness of Galton boards of any size.

In this study, the origin of our coordinate system is set to the center of the entrance. In other words, particles are launched from the entrance: the region $-1 + r < x < 1 - r$ and $y = 0$. The initial state of a particle is determined by the initial position and the initial velocity (x_0, v_0, θ_0), where v_0 denotes the magnitude of the velocity and θ_0 denotes the angle between the $-y$ direction and the velocity. Since the energy of particles considered here is constant, the initial state can be described by the two degrees of freedom (x_0, θ_0). The final state is defined as the position of the particle when it first crosses the line $y = -\sqrt{3}$, and the final state is assigned a symbol S_f, with a value of 1 if $x > 0$ and -1 if $x < 0$.

In the case of the first row of a Galton board it is reasonable to assume that the velocity is zero at the entrance. If the initial velocity is zero, the particles cannot leave the model via the entrance; that is, the entrance cannot be an exit. We describe the case of the positive initial momentum in Appendix B.

III. FRACTAL BASIN STRUCTURE AND INITIAL UNCERTAINTY

A. Fractal basin structure

The equation of motion which determines trajectories of particles connects an initial state to a coarse-grained exit state with the symbol $S_f = \pm 1$. The sets of initial states mapped onto the coarse-grained exit state $S_f = 1$ are the basin of the right exit, while the sets of initial conditions mapped onto the coarse-grained exit state $S_f = -1$ are the basin of the left exit.

Figure 3 shows the basins of the initial conditions for various radii of circular disks. A particle with an initial state in the white region leads to the left exit ($S_f = -1$), and a particle with an initial state in the black region leads to the right exit ($S_f = 1$). Since the initial velocity v_0 is zero, the basin structure is independent of the initial velocity angle θ_0, and the shapes of the basins are stripes. The widths of the stripes vary largely. In the case of $r = 0.50$ there are wide stripes compared with larger scatterer cases, and we can see the tendency that widths of stripes are thinner as the radii of scatterers are bigger. Notice that the horizontal scales are finer as the radii are bigger, and thus, the actual widths for the large

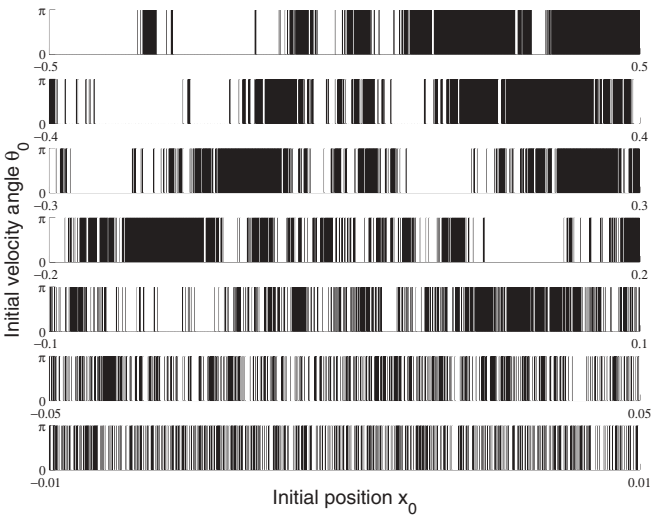

FIG. 3. Basin structures for radii $r = 0.50, 0.60, 0.70, 0.80, 0.90, 0.95$, and 0.99 (from above). The horizontal and vertical axes indicate the initial position x_0 and the initial velocity angle θ_0, respectively. The white and black regions show initial states of particles that pass out through the right ($S_f = 1$) and left ($S_f = -1$) exits, respectively.

radii are much thinner than they look in the figures. We can see that it is necessary to control initial states much more exactly in order to be able to determine the coarse-grained exit states for larger radii.

Figure 4 is a semilogarithmic plot of stripes' widths as a function of the radii. We clearly see that stripe widths are distributed over wide ranges, and the widths of the widest stripes decrease with the radii. The largest allowable uncertainty to control the results rapidly decreases as the radii approach 1. On the other hand, the widths of the thinnest stripes stay the same value for the same given resolution of the experiments.

It is worthwhile investigating the possibility that the basin structures are fractal since we can see some fractal-like structures in Fig. 3 and fractal basin boundaries can occur

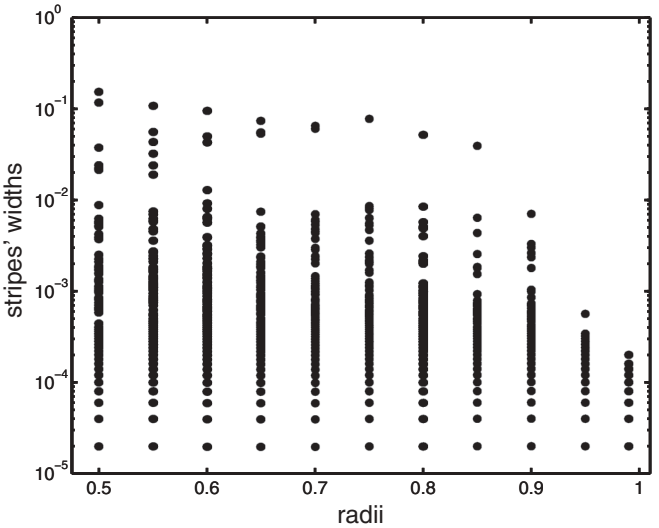

FIG. 4. Semilogarithmic plot of stripe widths as a function of the radii of the circular disks.

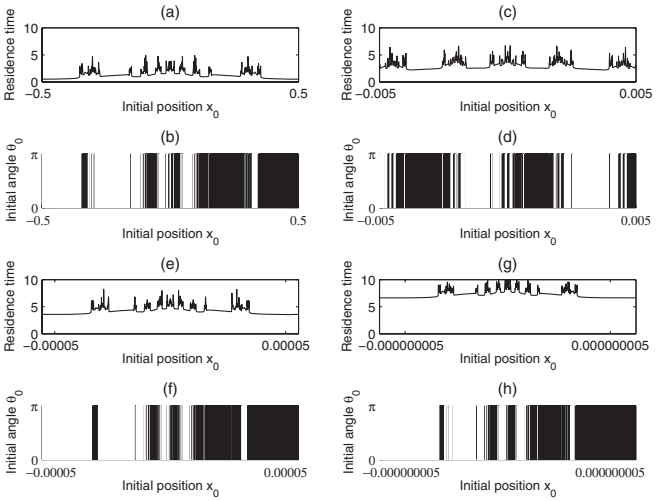

FIG. 5. (b), (d), (f), (h) Enlargements of the basin structures near the origin. (a), (c), (e), (f) Plot of the residence time corresponding to the enlarged basins.

for chaotic Hamiltonians with exits [23]. In addition, fractal basin structures with infinitely small structures can be an explanation for the constant width of the thinnest stripes' widths in Fig. 4. When we enlarge a region near $x_0 = 0$ in the case of $r = 0.50$, we can see the similar structures in every scale of Figs. 5(b), 5(d), 5(f), and 5(h). In addition, Figs. 5(a), 5(c), 5(e), and 5(f) show the residence time of particles in the scattering domain as a function of the initial positions, and the residence times are long and behave complicatedly in the segments where the basins have fine structures. These facts indicate that basins have fine structures near the origin.

For $r = 0.50$ in Fig. 3, we can see a fractal-like basin structure in many regions, not just around the origin. In Fig. 6, the enlargements of basins near $x_0 = 0.3$ show that there are fine structures, and this region also has fractal structures. On the other hand, the region around $x_0 = 0.2$, shown in

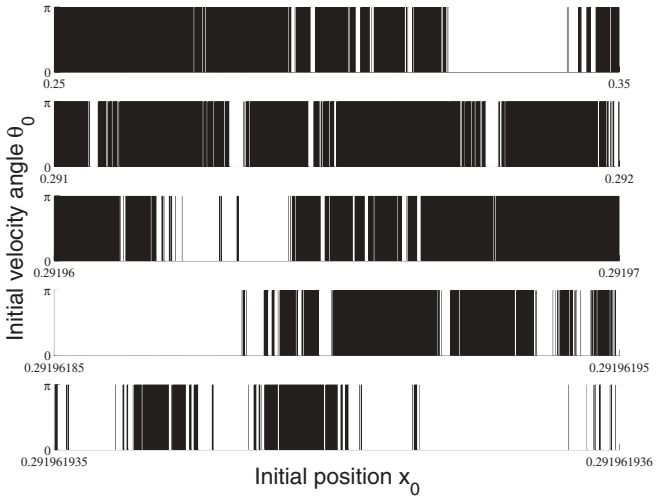

FIG. 6. Enlargements of the basin structures near 0.3 for $r = 0.50$. The ranges of x_0 are [0.25,0.35], [0.291,0.292], [0.29196,0.29197], [0.29196185,0.29196195], and [0.291961935,0.291961936].

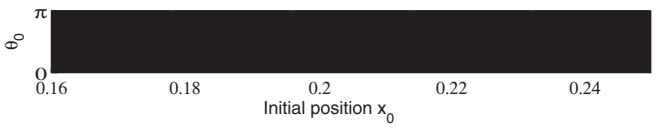

FIG. 7. Enlargements of the basin structures near 0.2 for $r = 0.50$.

Fig. 7, appears to be just one black basin. Sections with fine structure appear interleaved among such sections with no fine structure. Figure 8 shows the enlarged basin structures near the origin for $r = 0.99$ at various scales. For any enlarged figures, there are fine and similar structures, indicating the basins of $r = 0.99$ also have fractal structures. Similarly, for various radii of scatters, the basins have interleaved regions of fractal structures and nonfractal structures.

Let us compare the basin structure of a Galton board with those of coin tossing and dice throwing. Since there is no energy dissipation in our Galton board model, infinitely long trajectories can be produced, and there can exist infinitely fine structures. For example, the trajectory starting from the exact origin is an unstable periodic orbit and has an infinite residence time. There exist trajectories with very long residence times in the neighborhood of the origin. The trajectories with long residence times are related to the fine structures of basins since small differences between trajectories can become large over long times. The unstable periodic orbits, corresponding to the motion of particles which never escape from the domain, are thought to be related to the boundaries of basins. On the other hand, in the case of coin tossing and dice throwing, there is no infinite structures of basins since coins and dice settle into final states within finite time because of energy losses. Therefore, if initial uncertainty is small enough, we can, in principle, control the final states completely. However, it is worthwhile noting that, as the dissipation is smaller, the basins become finer and, in the limit of small dissipation, trajectories become long and the basin structures approach fractal [13,15]. It is difficult to introduce a method to determine the output states in ideal models of coin tossing and dice throwing without dissipation. In this sense, our model is in a different category from coin tossing and dice throwing models. In Appendix A, we use a

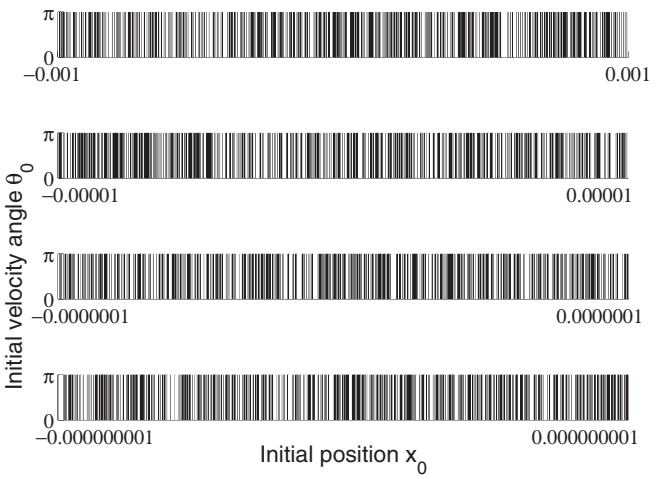

FIG. 8. Enlargements of the basin structures near origin for $r = 0.99$.

one-dimensional model to illustrate the key different features between the Galton board model and a coin tossing or dice model. The fractal structures are also observed in the case of positive initial momentum; see Appendix B 1.

B. Initial uncertainty

Let us consider that one cannot set an initial state without uncertainty. The uncertainty in the output of the Galton board model is attributable only to the uncertainty of the initial state since the equations of motion are deterministic and the output coarse-grained exit states are easily distinguishable. In other words, if the coarse-grained exit states are to give uncertain results, it can only be because the initial states vary uncertainly. In order to analyze the uncertainty in the output, it is important to consider the relation between the size of basins and the size of uncertainty regions.

The above description of basin structure shows that there are some regions where the same coarse-grained exit state will be obtained even if there is some uncertainty in the initial state, and there are other regions where any small uncertainty will result in uncertain output. Let us indicate the initial state by $\boldsymbol{x}_0$ and assume that we know only that the initial state lies somewhere in the neighborhood $\mathcal{U}(\boldsymbol{x}_0)$ of $\boldsymbol{x}_0$. We call the initial state $\boldsymbol{x}_0$ the center of the initial state and the neighborhood $\mathcal{U}(\boldsymbol{x}_0)$ the uncertain region of the initial state. If all initial states in an uncertain region $\mathcal{U}(\boldsymbol{x}_0)$ go to the same coarse-grained exit state, one will always get the same output S_f, even with the initial uncertainty. In this sense the output is predictable. On the contrary, if the uncertain region $\mathcal{U}(\boldsymbol{x}_0)$ spreads across the basins of both the coarse-grained exit states 1 and -1, we cannot determine the output in advance. The coarse-grained exit state is unpredictable in this case. When we say that our initial center $\boldsymbol{x}_0$ is uncertain by an amount ϵ, this means that what we really know is only that the initial condition lies somewhere in the uncertain region $|\boldsymbol{x} - \boldsymbol{x}_0| \leqslant \epsilon/2$, or $\mathcal{U}_\epsilon(\boldsymbol{x}_0) = \{\boldsymbol{x} : |\boldsymbol{x} - \boldsymbol{x}_0| \leqslant \epsilon/2\}$.

Let us consider the probabilities of the coarse-grained exit states as a function of ϵ. Figure 9 shows probabilities for exiting through the right side ($S_f = 1$). The probabilities stay around 0.5 in the case that $r = 0.99$ and $x_0 = 0$. The coarse-grained exit states remain unpredictable as the initial uncertainty decreases. Another example is the case where $r = 0.50$ and $x_0 \sim 0.3$, where the probabilities fluctuate strongly. The results for this case show that in some cases, even though we cannot predict coarse-grained exit states completely, we can predict the coarse-grained exit state with high probabilities. In this paper, we consider two meanings of the unpredictability: one is that there are possibilities for multiple outputs, as discussed in Sec. IV, and the other is that the probabilities for all outputs are even, as discussed in Sec. V.

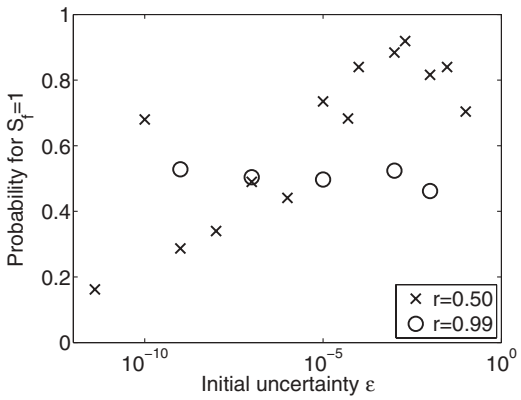

FIG. 9. Probabilities for exiting through the right side ($S_f = 1$) for various initial uncertainties ϵ. Two cases are shown, one with $r = 0.50$, $x_0 = 0$ and one with $r = 0.99$, $x_0 \sim 0.3$.

IV. FINAL STATE SENSITIVITY

In this section, we consider the unpredictability of the Galton board model in the sense that there is a possibility to reach either of the two coarse-grained exit states given a particular initial center x_0 and an amount ϵ of an uncertainty. The unpredictability is affected by the density of basin boundaries. In order to characterize the fractal structure of basin boundaries, we examine the Hausdorff dimension D_H of basin boundaries:

$$D_H \sim -\frac{\log N(l)}{\log l}, \tag{5}$$

where l is a length of a segment and $N(l)$ denotes the number of segments needed to cover the set of all basin boundaries. Figure 10 is a logarithmic plot of $N(l)$ as a function of l for $r = 0.50$, 0.60, 0.80, 0.90, and 0.99. We fitted the lines to $N(l)$ by applying the least mean square method to the short segment ranges, and the fitted lines are shown together in Fig. 10. Their slopes indicate the Hausdorff dimension D_H, and they are approximately 0.507, 0.567, 0.742, 0.853, and 0.991 for $r = 0.50$, 0.60, 0.80, 0.90, and 0.99, respectively. We can say that the dimensions of basin boundaries increase as the radii of scatterers increase.

Next, in order to characterize this kind of unpredictability we examine the sensitivity of the final states, in the sense

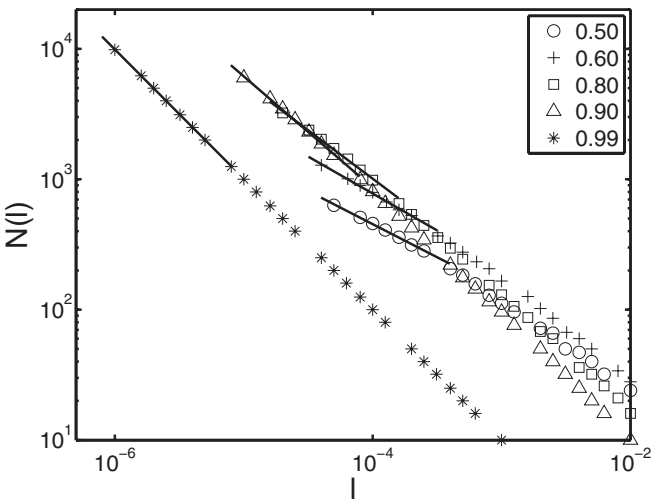

FIG. 10. Plot of the number $N(l)$ of segments covering all basin boundaries as a function of segment lengths l. The lines are calculated with the least mean square error, and their slopes indicate the Hausdorff dimension of basin boundaries. The slopes are 0.507, 0.567, 0.742, 0.853, and 0.991 for $r = 0.50$, 0.60, 0.80, 0.90, and 0.99, respectively.

of the sensitivity described in [24]. We know for sure that an initial condition goes to coarse-grained exit state 1 if $\mathcal{U}_\epsilon(\boldsymbol{x}_0)$ is included in the basin of $S_f = 1$. In this case, we say that an initial center x_0 is ϵ certain. On the other hand, if $\mathcal{U}_\epsilon(\boldsymbol{x}_0)$ consists of both $S_f = \pm 1$ basins, we cannot predict with absolute certainty whether the coarse-grained exit state is 1 or -1. In this case we say that the initial center x_0 is ϵ uncertain. An output corresponding to an initial region $\mathcal{U}_\epsilon(\boldsymbol{x}_0)$ is unpredictable, if the initial uncertainty ϵ is greater than or equal to ϵ_0 and the initial center $\boldsymbol{x}_0$ is ϵ_0 uncertain. The unpredictability of an initial state depends on the initial center and the value of ϵ; for example, while outputs are predictable for a sufficiently small ϵ in the nonfractal areas, they can be unpredictable for the same ϵ in the fractal areas. We introduce the ratio of unpredictable initial center for given ϵ as a measure of the unpredictability of the Galton board. Clearly, initial centers that are ϵ uncertain are those which lie within a distance ϵ of a basin boundary. If we were to pick an initial center at random, the probability of obtaining an ϵ uncertain initial center is the fraction of the area of the initial state space which lies within ϵ of a boundary. We call this fraction the final state sensitivity and denote it by $f(\epsilon)$. For a simple nonfractal boundary in a two-dimensional space of the initial conditions, $f(\epsilon)$ scales linearly with ϵ, or $f(\epsilon) \sim \epsilon$. However, when the boundaries are fractal, $f(\epsilon)$ has a different scaling with ϵ:

$$f(\epsilon) \sim \epsilon^\gamma, \tag{6}$$

$$\gamma = N - D_H, \tag{7}$$

where N is the phase space dimension and D_H is the Hausdorff dimension of the basin boundaries. Figure 11 shows $f(\epsilon)$ plotted on log-log axes, obtained from numerical experiments. The straight line fits indicate that f scales as a power of ϵ. The slope of the line gives the power γ. The results are 0.438, 0.387, 0.288, 0.158, and 0.007 for $r = 0.50$, 0.60, 0.80, 0.90, and 0.99, respectively. Note that Eq. (7) is approximately satisfied by the experiments shown in Figs. 10 and 11. As the radii increase, the Hausdorff dimension increases and the exponent γ of the final state sensitivity decreases. For large radii, basin boundaries become dense, and the probability, in the sense of the ratio of neighborhood regions $\mathcal{U}(\boldsymbol{x}_0)$ which has basins of two coarse-grained exit states, becomes high. For example, the probability is more than 80% when an amount ϵ of initial uncertainty approximately is more than 2–3 $\times 10^{-4}$ for $r = 0.9$, 0.01 for $r = 0.8$, or 0.05 for $r = 0.5$. The sensitivity increases, and so the predictability decreases, with ϵ according to a fractal scaling law, with an exponent that increases with the radius of the scatterer.

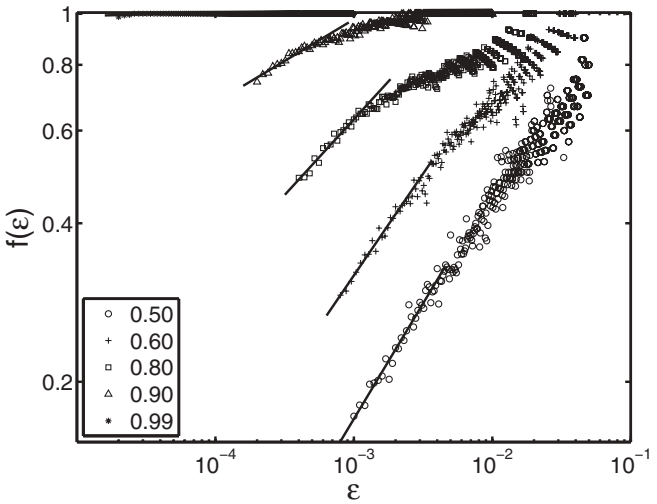

FIG. 11. Logarithmic plot of $f(\epsilon)$. The lines are calculated with the least mean square error, and their slopes indicate the exponents of the final state sensitivity γ. The slopes are 0.438, 0.387, 0.288, 0.158, and 0.007 for $r = 0.50$, 0.60, 0.80, 0.90, and 0.99, respectively.

V. STATISTICAL BIAS OF THE FINAL STATE

In this section, we discuss the unpredictability from the viewpoint of statistical bias. When the proportions of areas of two basins in the initial uncertain region are biased, the proportions of the two final states obtained for uniformly random choices of initial states are also biased, and we can say that the final states become somewhat more predictable than if the proportions were equal. For the two final states $S_f = \pm 1$, the statistical bias of the final states can be defined as the averaged value of the final states. Suppose that initial conditions are uniformly distributed within the uncertain regions $\mathcal{U}_\epsilon(\boldsymbol{x}_0)$ of the width ϵ. We denote $\langle S_f \rangle_{\epsilon, \boldsymbol{x}_0}$ as the averaged final state S_f over the uncertain region $\mathcal{U}_\epsilon(\boldsymbol{x}_0)$ for given $\boldsymbol{x}_0$.

First, we show the distributions $p(\langle S_f \rangle_\epsilon)$ of the averaged final states when the centers of the initial uncertainty are chosen at random in the entrance of the scattering domain. Figure 12 shows the histograms $p(\langle S_f \rangle_\epsilon)$ for $r = 0.50$. The averaged final states $\langle S_f \rangle_\epsilon$ are sharply distributed around the origin in the case that the initial uncertainty width is almost the same as the width of the entrance, that is, $\epsilon \sim 2(1 - r)$. This means that the probability of the final states $S_f = \pm 1$ is even, and we cannot at all predict coarse-grained exit states wherever the initial center is. When the width ϵ is smaller than the entrance, the distribution of $\langle S_f \rangle_\epsilon$ broadens and has multiple peaks. This means that the fluctuation of $\langle S_f \rangle_\epsilon$ becomes large and the probabilities of the final states are strongly biased for

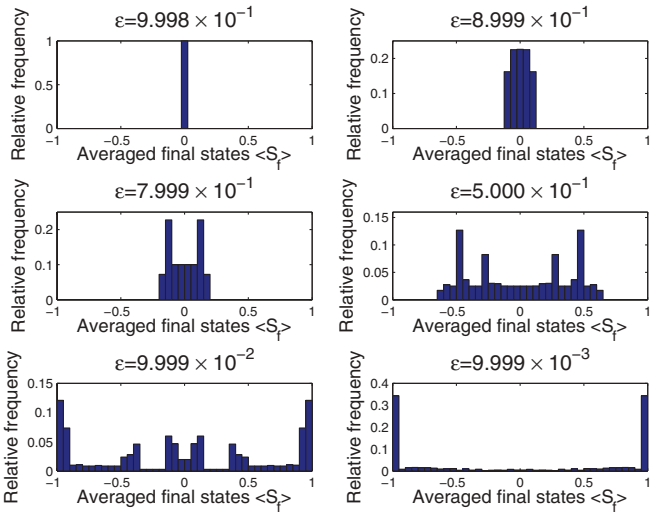

FIG. 12. (Color online) Histograms of the averaged final states $\langle S_f \rangle$ for various sizes of the uniform uncertainty in the case of $r = 0.50$. The vertical axes indicate relative frequency.

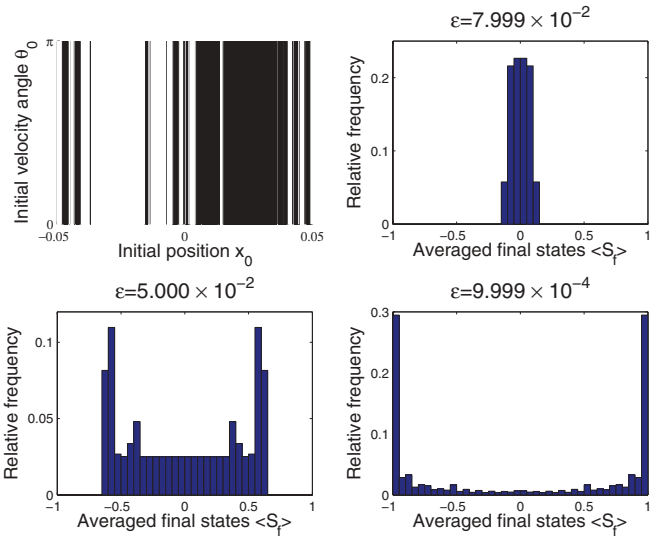

FIG. 13. (Color online) Enlarged basin structures (top left) and histograms of the averaged final states $\langle S_f \rangle$ for various sizes of the uniform uncertainty when the initial conditions are restricted to the region around the origin $[-0.05, 0.05]$ in case of $r = 0.50$.

large portions of the initial centers. When the width ϵ decreases further, peaks appear in the distribution at $\langle S_f \rangle_\epsilon = \pm 1$, so that even if we choose the center of initial condition at random, the outputs are predictable in almost all cases.

Next, we consider the distributions of $\langle S_f \rangle_\epsilon$ when the centers of the initial uncertainty are restricted to near the origin, where the structures of basins are fractal. The distributions of $\langle S_f \rangle_\epsilon$ behave in a way similar to the unrestricted case because of the self-similar nature of the fractal basin boundaries in Fig. 13. The distribution has a peak around $\langle S_f \rangle_\epsilon = 0$ when ϵ is large. As ϵ becomes smaller, the distribution broadens and finally has peaks around $\langle S_f \rangle_\epsilon = \pm 1$. Figure 14 shows the basin structures and the distribution of $\langle S_f \rangle_\epsilon$ when the initial conditions are restricted to the region [0.29,0.3]. We can see fine basin boundary structures, but the areas of black are larger than the areas of white. As a result, the final state 1 occurs more frequently than -1, and $\langle S_f \rangle_\epsilon$ are very biased.

In the case of $r = 0.99$, the distribution of $\langle S_f \rangle_\epsilon$ has a peak at $\langle S_f \rangle_\epsilon = 0$ even when the width of the uncertainty is quite small compared to the entrance length 0.02, as shown in Fig. 15. This is different from the case of $r = 0.50$. However, as the width of the uncertainty is made even smaller, the distributions broaden and have a two peak structure, as seen in the case of $r = 0.50$. Comparing with $r = 0.50$, although there are two peaks, the peaks are low and are not at $\langle S_f \rangle_\epsilon = \pm 1$ but near the center $\langle S_f \rangle_\epsilon = 0$. This means that there are some biases in the appearance of final states, but they are small. The width of the initial uncertainty required to acquire unbiased outcomes is much smaller than that for $r = 0.50$.

Next, we consider the variance v_{Sf} of the statistical bias $\langle S_f \rangle_\epsilon$. Figure 16 shows the variances v_{Sf} as a function of the widths ϵ of the initial uncertainty for $r = 0.50$ (top left), 0.90 (top right), and 0.99 (bottom left). As the uncertainty ϵ increases, the variance decreases. When the uncertainty becomes the same as the length of the entrance, the variance finally becomes zero, which means that almost all $\langle S_f \rangle_\epsilon$ localize near zero due to the symmetry of the layout of the Galton board model. The larger the radius is, the smaller the variance is for the same ratio of the uncertainty width to the entrance width. We regard the uncertainty widths at which the variance becomes a certain value $v_c = 0.01$ as the unbiased uncertainty size w_c. The bottom right plot in Fig. 16 shows w_c as a function of the radii r. Thus, we can determine the radii and uncertainty of initial conditions required to achieve a given variance. For example, a small bias ($v_{Sf} < 0.01$) is achieved with $\epsilon \sim 0.1$ for $r = 0.9$, $\epsilon \sim 0.3$ for $r = 0.8$, or $\epsilon \sim 0.85$ for $r = 0.5$. In general, we can see the tendency that w_c becomes smaller as the radii become bigger.

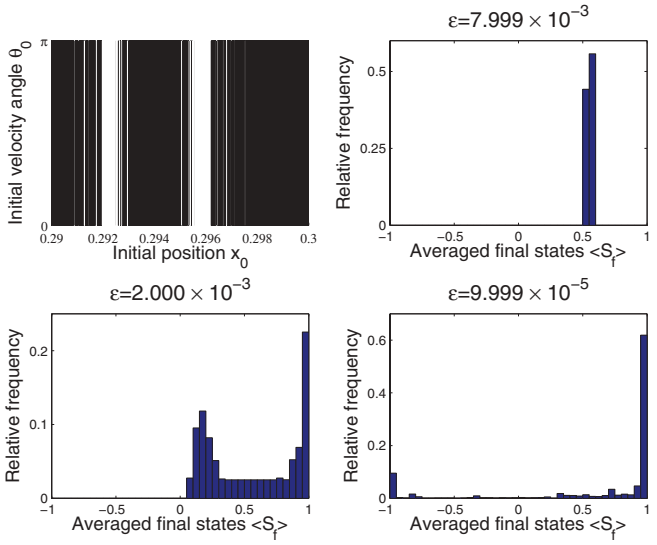

FIG. 14. (Color online) Enlarged basin structure (top left) and histograms of the averaged final states $\langle S_f \rangle_\epsilon$ for various sizes of the uniform uncertainty when the initial conditions are restricted to the region [0.29,0.3] in the case of $r = 0.50$.

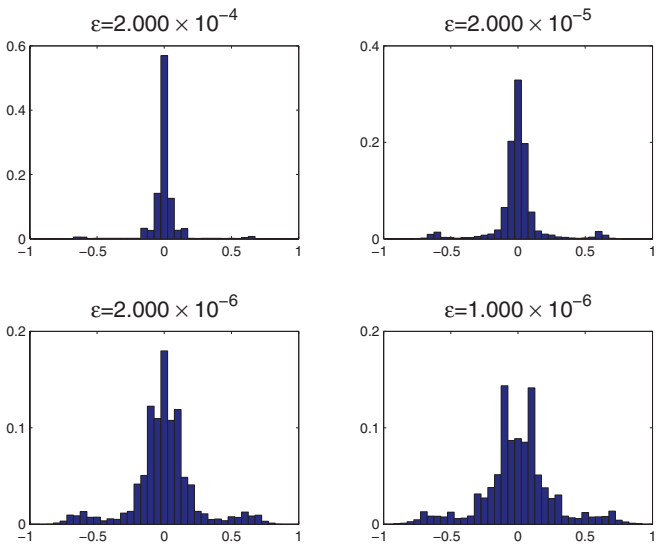

FIG. 15. (Color online) Histograms of the averaged final states $\langle S_f \rangle_\epsilon$ for various sizes of uniform uncertainty in the case of $r = 0.99$. The vertical axes indicate relative frequency.

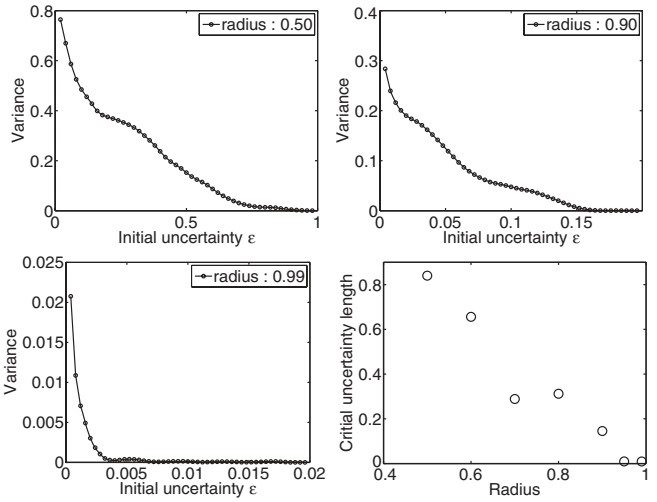

FIG. 16. Variance v_{Sf} of the final states as a function of the initial uncertainty for $r = 0.50$ (top left), 0.90 (top right), 0.99 (bottom left). Critical uncertainty length for radii where the variance v_{Sf} of the final states is 0.01 (bottom right).

It is noted that the fraction $f(\epsilon)$, which we call the final state sensitivity, indicates Prob($S_f \neq \pm 1$) and the scaling γ determines how fast Prob($S_f \neq \pm 1$) approaches zero for small ϵ. In this sense, the statistical distribution of statistical bias $\langle S_f \rangle_\epsilon$ is related to the final state sensitivity. The results of the statistical bias with positive initial momentum are described in Appendix B 2.

VI. SUMMARY AND DISCUSSION

We reported about the mechanism for the manifestation of randomness in the motion of particles in a Galton board model. There are two aspects in the Galton board model. One is determinism: the motions of particles in the Galton board model are governed by the deterministic equations. The other is nondeterminism: initial states of particles have inevitable uncertainty due to the fluctuation and inaccuracy of the initial setups of particles. We focused on the effects of the initial uncertainty on the unpredictability of coarse-grained output states, that is, exit channels, because, assuming that initial setups are independent trials, the unpredictability is the key feature for the randomness of the output states. From point of view of clarifying the conditions for unpredictability, it is beneficial to investigate the structures of basins in the initial state space corresponding to the output states since the relative sizes of the initial uncertainty and the basins is significantly related to the unpredictability.

The basins of our Galton board model without energy dissipation have infinitely fine and self-similar structures with fractal boundaries. This characteristic affects the unpredictability of output states. The output states of the Galton board model, the exit channels, are determined independently of any dissipation. This is an important difference compared to coin tossing or dice throwing models. The coin tossing and dice throwing models require dissipation in order to determine the output states and so cannot have fractal structure.

We discussed two kinds of unpredictability in this paper. One is the case where there is the possibility of two output states. The other is the case where the probability of the two output states is equal. We refer to the former as weak unpredictability and the latter as strong unpredictability. In this paper, these two kinds of unpredictability are analyzed by introducing two statistical measures, final state sensitivity and distribution of statistical bias.

The weak unpredictability is characterized by the final state sensitivity, which indicates how ubiquitously the infinite fine structures exist in the whole initial space, more specifically how fast the probability that the region of initial uncertainty contains different basins decays as the amount of initial uncertainty decreases. As the radii of circular disks increase, the probability decays more slowly, which means that the weak unpredictability is enhanced for large disks.

The strong unpredictability is characterized by statistical bias and its variation. The variation of statistical bias is related to the robustness of distributions of final states. The variance of the averaged output values indicates the fluctuation of the statistical bias when an initial state is uniformly picked up from initial space, and a small variance means that the minute basin structure becomes homogeneous over the whole initial space. Our numerical experiments showed that the variance of statistical bias is a function of radii r and the variance decreases as radii increase. Therefore, if the variance is regarded as the specified quality of randomness, for a given initial uncertainty, we can determine the critical r which achieves the quality of randomness. All of these results amount to saying that the Galton board model becomes a better randomizer the larger the radii of disk scatterers are.

Although the primary purpose of this study is to analyze the properties of the idealized two-dimensional small mathematical model of the Galton board, let us briefly comment on what the results indicate about the effect of some properties of real Galton boards on randomness. First, our model has no energy dissipation, which can produce long trajectories and fine basins, and these greatly influence the unpredictability. If you carefully make a Galton board with well chosen materials, the behavior of the real Galton board will be well approximated by our idealized model. Second, we neglected the environmental fluctuations which perturb a ball during its motion. By the perturbation, the basin structures become blurred, especially for minute basin structure, and the unpredictability of the

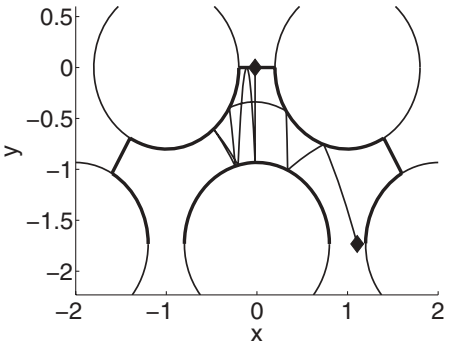

FIG. 17. Small Galton board model for $r = 0.80$. The bold lines show reflecting surfaces in the model, and there is an additional straight reflecting surface at the entrance in the case of positive initial momentum.

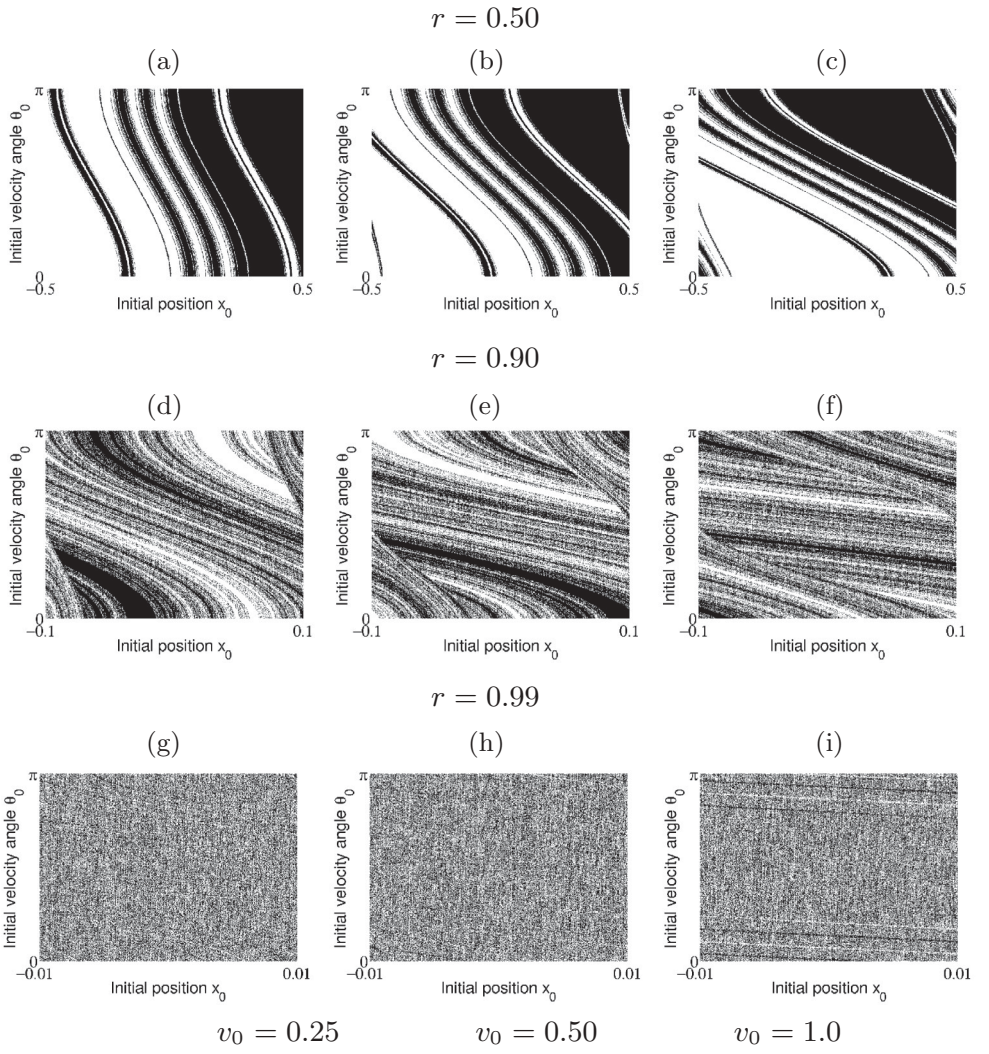

FIG. 18. Basin structures. The horizontal axis shows the initial particle position x_0 ($\in [r-1, 1-r]$), and the vertical axis shows the angle θ_0 ($\in [0,\pi]$) of the initial velocity. White shows the basin of the coarse-grained exit state ($S_f = 1$), and black shows the basin of the coarse-grained exit state ($S_f = -1$). Left: $v_0 = 0.25$, middle: $v_0 = 0.50$, and right: $v_0 = 1.0$. (a)–(c) $r = 0.50$, (d)–(f) $r = 0.90$, and (g)–(i) $r = 0.99$.

output states may increase. Third, we investigated only a small Galton board model instead of a large sized model with multiple layers and multiple exit channels. We can conjecture that the large sized models still have the same important characteristics for the randomness, such as the fractal basin structures and the behavior of statistical biases. The dynamical structures are unaltered whether a die is regular hexahedron or regular dodecahedron. Similarly, it seems reasonable to suppose that the essential characteristics of the dynamical structures of the large sized models remain the same as those of the small model.

APPENDIX A: ONE-DIMENSIONAL MODEL

Here, we discuss the difference between our Galton board model and a coin tossing model by using the following one-dimensional map:

$$M(x) = \begin{cases} 2\eta x, & \text{if} \quad x < 1/2, \\ 2\eta x - \eta, & \text{if} \quad x > 1/2. \end{cases}$$

Although the map is an abstract model, it can express the core features of random number generation mechanisms for the Galton board and coin tossing, and it is expedient to accentuate the differences between them. For $\eta = 1$, the map is the Bernoulli map, mapping $[0,1]$ onto $[0,1]$. We consider the rough assumption for coin tossing that the initial energy is fixed and the loss of energy for one bounce is constant, so that a coin comes to rest at heads or tails after a fixed number of bounces under our assumption. Then we can think of the result of a coin toss as corresponding to the final state of the one-dimensional mapping after a fixed number of iterations. For $\eta > 1$, there are two windows, $[\frac{1}{2\eta}, \frac{1}{2}]$ and $[\frac{1}{2} + \frac{1}{2\eta}, 1]$, through which trajectories of x can escape from the region $[0,1]$. Once trajectories enter in the windows, they get mapped into the region $x > 1$ and move toward ∞ on successive iterations. If we consider that a final state is determined by which window a trajectory passes through, then we can think of this one-dimensional model as corresponding to our Galton board model. Almost all initial conditions in $[0,1]$ eventually go to

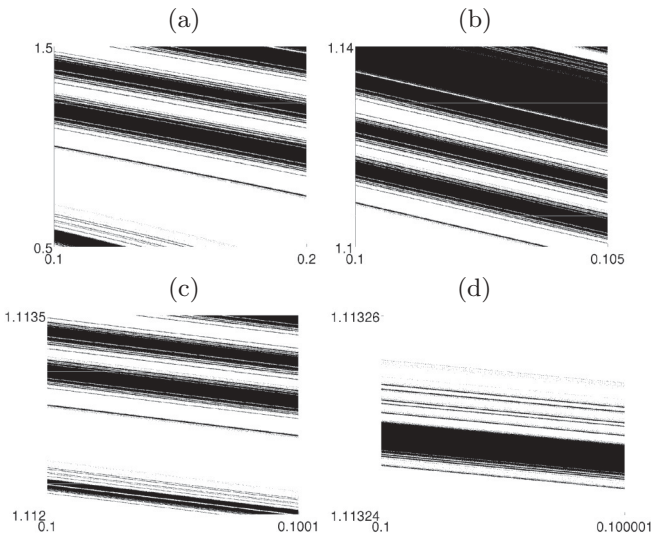

FIG. 19. Enlarged basin structures for $r = 0.50$: (a) $0.1 \leqslant x \leqslant 0.2$ and $0.5 \leqslant \theta \leqslant 1.5$, (b) $0.1 \leqslant x \leqslant 0.105$ and $1.1 \leqslant \theta \leqslant 1.14$, (c) $0.1 \leqslant x \leqslant 0.1001$ and $1.112 \leqslant \theta \leqslant 1.1135$, and (d) $0.1 \leqslant x \leqslant 0.100001$ and $1.11324 \leqslant \theta \leqslant 1.11326$.

infinity. However, there are infinitely long trajectories which never get out. The measure of such remaining trajectories is zero, and these trajectories have fractal structures and become basin boundaries. We note that these basin structures are similar to that of our Galton board model, and the behaviors can be regarded as chaotic scattering. The dimension of basin boundaries becomes larger as η becomes small in the same way the dimension becomes larger as the radii of scatterers become larger. This is similar to the way that fractal basin boundaries and infinitely small size of basins are formed in our Galton board model. The predictability of the final states for arbitrarily small initial uncertainty depends on whether the position of the initial centers is in fractal regions or not.

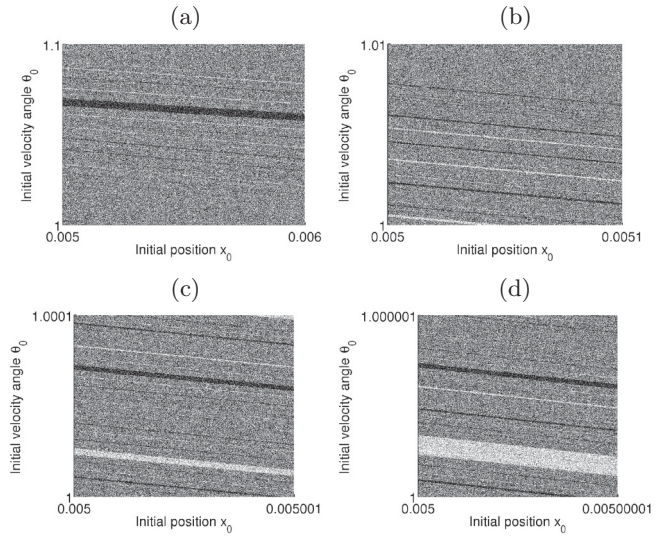

FIG. 20. Enlarged basin structures for $r = 0.99$: (a) $0.05 \leqslant x \leqslant 0.006$ and $1 \leqslant \theta \leqslant 1.1$, (b) $0.05 \leqslant x \leqslant 0.0051$ and $1 \leqslant \theta \leqslant 1.01$, (c) $0.05 \leqslant x \leqslant 0.005001$ and $1 \leqslant \theta \leqslant 1.0001$, and (d) $0.05 \leqslant x \leqslant 0.00500001$ and $1 \leqslant \theta \leqslant 1.000001$.

APPENDIX B: POSITIVE INITIAL MOMENTUM

In this section, we consider the case where the initial velocity has a positive value. In order to prevent particles with nonzero initial velocity from escaping from the scattering domain through the entrance, we assume an additional straight reflecting surface between the circular disks, as shown in Fig. 17.

1. Fractal basin structure

As shown in Fig. 18, as the radii of scatterers become larger, the basin structure becomes finer in the same way as for particles with the zero initial velocity case. However, due to the initial velocity, the structures of basins are twisted and skewed.

The basin boundaries appear to be fractal in this case too. To check the possibility of fractal basins, the appropriate

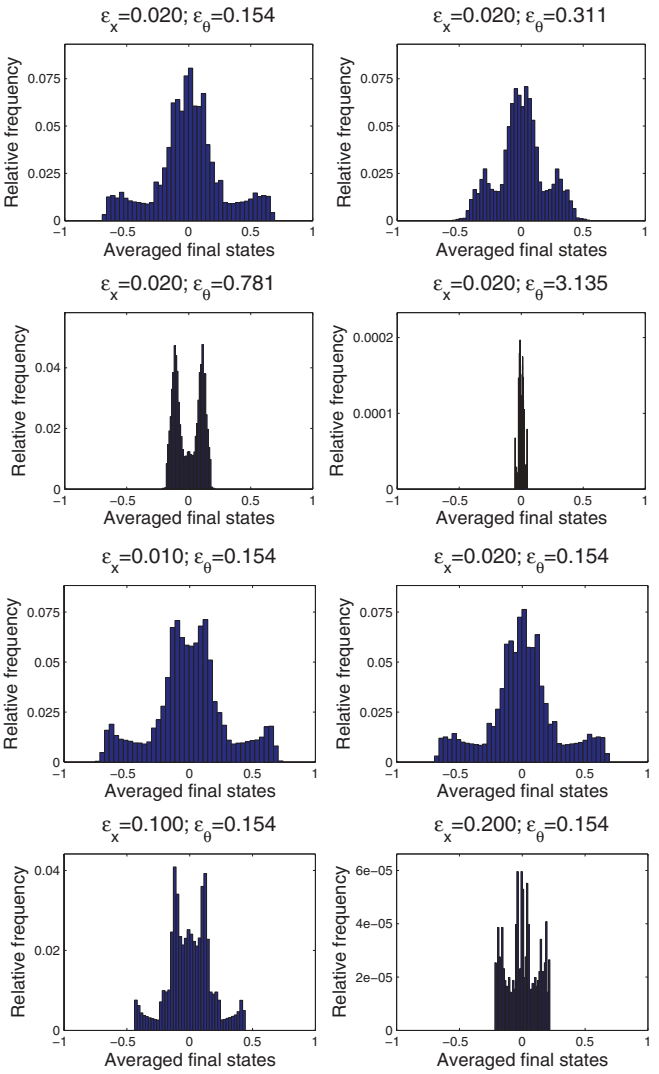

FIG. 21. (Color online) Distribution of the averaged final state $\langle S_f \rangle_\epsilon$ for $r = 0.90$ and $v_0 = 1.0$. The top four plots show histograms for various uncertainties ϵ_θ of the initial velocity angles when uncertainty ϵ_x of the initial positions is fixed, and the bottom four plots are for various ϵ_x when ϵ_θ is fixed. The vertical axes indicate relative frequency.

enlargements are presented in Fig. 19 ($r = 0.50$) and Fig. 20 ($r = 0.99$). Under further magnification new finer structures can be resolved, and the boundaries appear to be fractal. These fractal basin boundaries indicate infinitely complicated relationships between initial states and final states, which are typical of chaotic scattering.

2. Statistical bias

In this section, we investigate the statistical bias for initial conditions with nonzero velocity. Here, we consider the uncertainty of the initial velocity as well as the initial position. Figure 21 shows the distribution of statistic bias $\langle S_f \rangle_\epsilon$ of $r = 0.90$ for various uncertainties of initial position ϵ_x and initial velocity angle ϵ_θ. The four top plots show various ϵ_θ and fixed ϵ_x (=0.0198). As the uncertainty ϵ_θ becomes smaller, the distributions become broader, with multiple peaks. For large velocity angle uncertainties, the distributions are narrow, with a single peak at $\langle S_f \rangle_\epsilon = 0$. The four bottom plots show results for various ϵ_x and fixed ϵ_θ (=0.154). Even though the uncertainty ϵ_x is large, the distribution is still broad, with multiple peaks. The fixed uncertainty ϵ_θ is too small to get unbiased statistics of the final states. For these parameter values, sometimes the outputs are biased and sometimes the outputs are unbiased, depending on the initial center state. Figure 22 shows the distributions of the averaged final state $\langle S_f \rangle_\epsilon$ for $r = 0.50$ and 0.99 for various ϵ_x and fixed ϵ_θ. For $r = 0.50$, the distributions are very wide, and they have peaks on both sides. In this case, the outputs are strongly biased almost everywhere. The angle uncertainty ϵ_θ is too small to get peaky distributions. As seen in Fig. 18, basins are blocky for $r = 0.50$, and this is the cause of these multipeak distributions. For $r = 0.99$, the distributions of $\langle S_f \rangle_\epsilon$ are not so wide, even when the uncertainty is comparably small. However, we can see fluctuation around $\langle S_f \rangle_\epsilon = 0$ even for large ϵ_x.

Figure 23 shows the variance of $\langle S_f \rangle_\epsilon$ as a function of the uncertainty for $r = 0.50$, 0.60, 0.70, 0.80, 0.90, 0.95, and

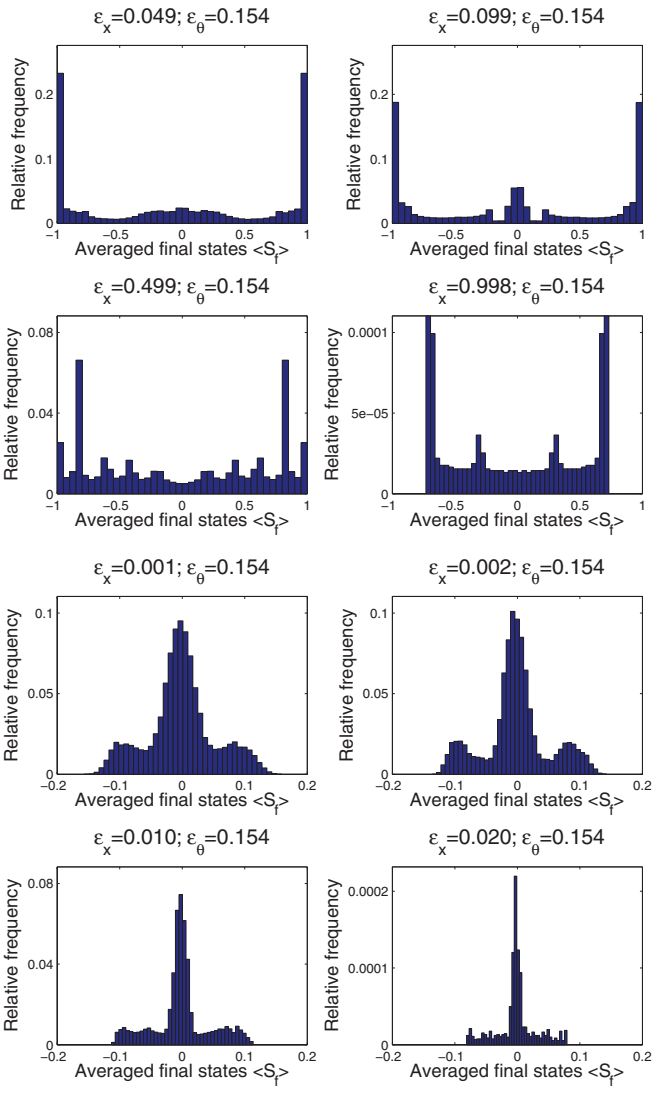

FIG. 22. (Color online) Distribution of the averaged final states $\langle S_f \rangle_\epsilon$ for $r = 0.50$ (top four plots) and 0.99 (bottom four plots). The uncertainty ϵ_θ is fixed at 0.154. The vertical axes indicate relative frequency.

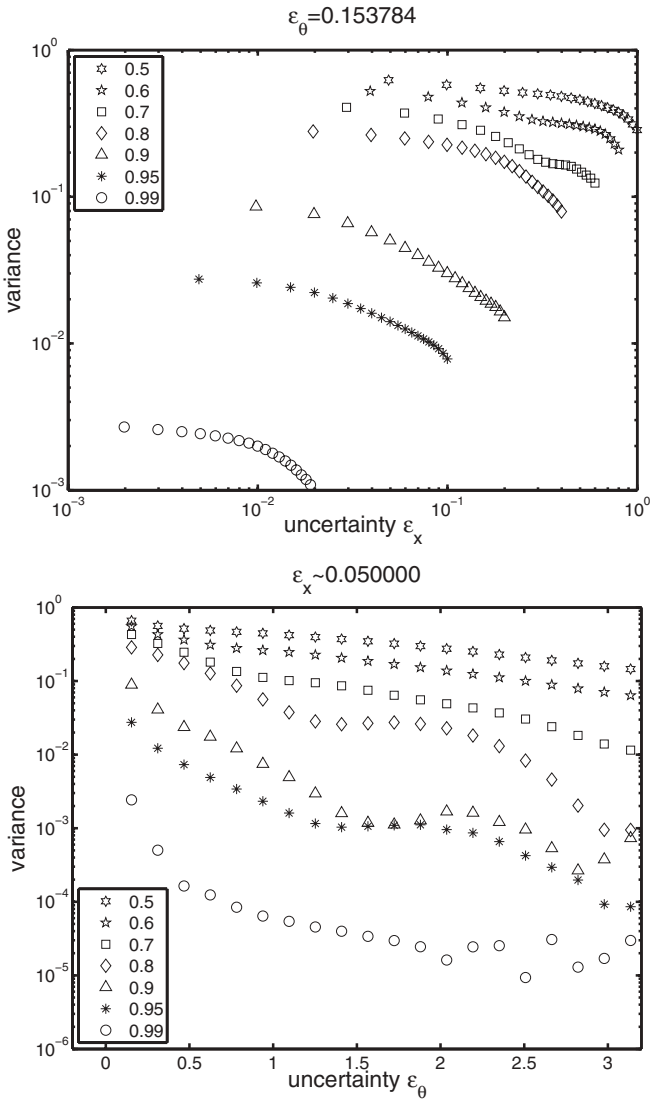

FIG. 23. Variance of $\langle S_f \rangle_\epsilon$ as a function of the uncertainty for $r = 0.50$, 0.60, 0.70, 0.80, 0.90, 0.95, and 0.99: (top) ϵ_θ is fixed at 0.154 and ϵ_x varies; (bottom) ϵ_x is fixed at 0.050 and ϵ_θ varies.

0.99. In the top panel of Fig. 23, the variances of $\langle S_f \rangle_\epsilon$ are shown when the uncertainty ϵ_θ of the initial angles is fixed. As the uncertainty ϵ_x for the initial position decreases, the variance of the average final state increases. In the case of $r = 0.50$, the variance is 0.3 even if the uncertainty is maximum. The uncertainty of the initial angle is too small to get the narrow distributions. As the radii become large, the variance decreases. The bottom panel of Fig. 23 shows the variance of $\langle S_f \rangle_\epsilon$ when the uncertainty ϵ_x of the initial position is fixed. As the uncertainty for initial angles increases, the variance of the final states decreases. In the case of $r = 0.50$, when the uncertainty for the initial position is π, the variance of the mean final states is 0.2 due to the uncertainty of the initial positions. We can see that in order for the final states to be more unpredictable, the uncertainty should be larger and the radii should become larger.

[1] A. Menezes, P. Van Oorschot, and S. Vanstone, *Handbook of Applied Cryptography* (CRC Press, Boca Raton, FL, 1997).

[2] N. Meteopolis and S. Ulam, J. Am. Stat. Assoc. **44**, 335 (1949).

[3] S. Asmussen and P. Glynn, *Stochastic Simulation: Algorithms and Analysis* (Springer, New York, 2007).

[4] D. Knuth, *The Art of Computer Programing*, 3rd ed. (Addison-Wesley, Reading, Massachusetts, 1998), Vol. 2, pp. 10–26.

[5] M. Matsumoto and T. Nishimura, ACM Trans. Model. Comput. Simul. **8**, 3 (1998).

[6] A. Uchida, K. Amano, M. Inoue, K. Hirano, S. Naito, H. Someya, I. Oowada, T. Kurashige, M. Shiki, S. Yoshimori, K. Yoshimura, and P. Davis, Nat. Photonics **2**, 728 (2008).

[7] T. Harayama, S. Sunada, K. Yoshimura, P. Davis, K. Tsuzuki, and A. Uchida, Phys. Rev. A **83**, 031803(R) (2011).

[8] S. F. Galton, *Natural Inheritance* (Macmillan, New York, 1889).

[9] M. Kac, Sci. Am. **211**, 92 (1964).

[10] J. B. Keller, Am. Math. Mon. **93**, 191 (1986).

[11] V. Z. Vulović and R. E. Prange, Phys. Rev. A **33**, 576 (1986).

[12] P. Diaconis, S. Holmes, and R. Montgomery, SIAM Rev. **49**, 211 (2007).

[13] J. Strzalko, J. Grabski, A. Stefanski, P. Perlikowski, and T. Kapitaniak, Phys. Rep. **469**, 59 (2008).

[14] M. Clark and B. Westerberg, Can. Med. Assoc. J. **181**, E306 (2009).

[15] J. Strzalko, J. Grabski, A. Stefanski, P. Perlikowski, and T. Kapitaniak, Math Intell. **32**, 54 (2010).

[16] J. Nagler and P. Richter, Phys. Rev. E **78**, 036207 (2008).

[17] B. Moran, W. Hoover, and S. Bestiale, J. Stat. Phys. **48**, 709 (1987).

[18] W. Hoover, B. Moran, C. Hoover, and W. Evans, Phys. Lett. A **133**, 114 (1988).

[19] A. Lue and H. Brenner, Phys. Rev. E **47**, 3128 (1993).

[20] V. Kozlov and M. Mitrofanova, Regular Chaotic Dyn. **8**, 431 (2003).

[21] N. Chernov and D. Dolgopyat, Phys. Rev. Lett. **99**, 030601 (2007).

[22] F. Barra, P. Gaspard, and T. Gilbert, Phys. Rev. E **80**, 021127 (2009).

[23] S. Bleher, C. Grebogi, E. Ott, and R. Brown, Phys. Rev. A **38**, 930 (1988).

[24] E. Ott, in *Chaos in Dynamical Systems,* 2nd ed. (Cambridge University Press, Cambridge, 2002), pp. 175–178.

[25] P. Gaspard and S. Rice, J. Chem. Phys. **90**, 2225 (1989).

[26] T. Harayama and P. Davis, Opt. Lett. **23**, 1426 (1998).

[27] Class Library for Numbers, http://www.ginac.de/CLN/. CLN is a library for efficient computations with all kinds of numbers at arbitrary precision.